In vitro study of interaction of synaptic vesicles with lipid membranes

S K Ghosh[1]**, S Castorph**[1]**, O Konovalov**[2]**, R Jahn**[3]**, M Holt**[3] **and T Salditt**[1,4]

[1] Institute for X-ray Physics, University of Goettingen, 37077 Goettingen, Germany
[2] European Synchrotron Radiation Facility, 38043 Grenoble Cedex, France
[3] Department of Neurobiology, Max Planck Institute for Biophysical Chemistry, 37077 Goettingen, Germany
E-mail: sghosh1@gwdg.de, mholt@gwdg.de and tsaldit@gwdg.de

Abstract. The fusion of synaptic vesicles (SVs) with the plasma membrane in neurons is a crucial step in the release of neurotransmitters, which are responsible for carrying signals between nerve cells. While many of the molecular players involved in this fusion process have been identified, a precise molecular description of their roles in the process is still lacking. A case in point is the plasma membrane lipid phosphatidylinositol 4,5-bisphosphate (PIP_2). Although PIP_2 is known to be essential for vesicle fusion, its precise role in the process remains unclear. We have re-investigated the role of this lipid in membrane structure and function using the complementary experimental techniques of x-ray reflectivity, both on lipid monolayers at an air–water interface and bilayers on a solid support, and grazing incidence x-ray diffraction on lipid monolayers. These techniques provide unprecedented access to structural information at the molecular level, and detail the profound structural changes that occur in a membrane following PIP_2 incorporation. Further, we also confirm and extend previous findings that the association of SVs with membranes is enhanced by PIP_2 incorporation, and reveal the structural changes that underpin this phenomenon. Further, the association is further intensified by a physiologically relevant amount of Ca^{2+} ions in the subphase of the monolayer, as revealed by the increase in interfacial pressure seen with the lipid monolayer system. Finally, a theoretical calculation concerning the products arising from the fusion

[4] Author to whom any correspondence should be addressed.

of these SVs with proteoliposomes is presented, with which we aim to illustrate the potential future uses of this system.

Contents

1. Introduction

Eukaryotic cells are elaborately subdivided into functionally distinct, membrane-enclosed compartments. Each compartment, or organelle, contains its own characteristic set of enzymes and other specialized molecules, allowing a complex range of reactions both within these compartments and on the membrane surfaces. Communication between the different cellular compartments usually involves specialist transport vesicles, which bud from the precursor compartment and are delivered to the target membrane where they dock and fuse, delivering both membrane constituents and soluble content material from the donor to the acceptor compartment or to the extracellular space. Interestingly, budding and fusion are no longer seen as a passive consequence of cellular activity but depend upon a complex network of interactions between specialist proteins and lipids, which create membrane domains and organize centers for membrane trafficking.

While the last decade has seen a tremendous increase in our understanding of the molecular machinery involved in the budding and fusion of biological membranes, much less is known about the structural changes that underlie these processes, despite this being an essential aspect of the problem. Although usually thought of as the preserve of biochemists and cell biologists,

in our opinion it is likely that such a structural understanding will also need the combined input of researchers from fields as diverse as physics, chemistry and engineering.

In this paper, we present recent work from our laboratory in which we have taken three techniques already well established in the physics community and applied them to the study of membrane structure and function, in the hope that they will be able to shed new light on the structural changes that occur during fusion. As our model system, we chose synaptic vesicles (SVs). These vesicles are a specialized trafficking organelle found in the presynaptic terminal of neurons, where they store small chemical neurotransmitters. These vesicles fuse with the plasma membrane (exocytosis) in response to Ca^{2+} influx during neuronal stimulation, releasing the neurotransmitter into the synaptic cleft before being recycled (endocytosis) for subsequent reuse [1]. We chose to use SVs for three main reasons. Firstly, SVs are the only trafficking organelle that can be purified to apparent homogeneity in large quantities, making them highly amenable to experimental study. Secondly, the protein and lipid composition of the SV is better understood than any other organelle; models of the SV based mainly on our own biochemical data and from our work using small angle x-ray scattering (SAXS) have confirmed the main structural components and organizational principles (see figure 1 and text below) [2]–[4]. Furthermore, our knowledge of the SV extends to the increasingly complex network of interacting proteins and lipids that have been identified as regulating and executing exocytosis and endocytosis [1], [5]–[7]. For instance, of particular interest in exocytosis are the vesicular protein synaptotagmin (which is thought to be the calcium sensor on the SV) and its effector lipid phosphatidylinositol 4,5-bisphosphate (PIP$_2$), which resides in the plasma membrane [5]. Thirdly, the fusion of SVs in neurons occurs at specialist sites (active zones) on the presynaptic membrane, which are characterized by the complexity of their protein and lipid compositions [6]–[8]. By using isolated SVs with model membranes of defined lipid and protein composition, we hope to be able to circumvent the complexity of the *in vivo* situation in a way that allows us to successfully dissect out the roles of individual components of the fusion machinery.

Our strategy has been to first understand the structure of isolated SVs, before studying their interactions with model membranes. In this respect, the wealth of pre-existing information about these vesicles was invaluable in allowing us to establish 'proof-of-principle' for our own experimental systems. Here we present these data, as well as some new and exciting results we have obtained that provide unprecedented structural insights into the interaction of SVs with membranes.

Using the technique of SAXS, we have structurally characterized SVs and present a refined model of vesicle structure. Further, we address the possibility of SAXS being used to study the fusion of SVs with small proteoliposomes, with the ultimate goal of providing detailed structural information about the transitional intermediates that occur during the process. Next we have used two complementary planar membrane systems in an attempt to understand how SVs interact with the plasma membrane *in vivo*. The first of these systems is the single lipid bilayer, which is formed on a hydrophilic surface by the fusion of small unilamellar vesicles (SUV). Since its introduction in 1985, this solid supported lipid bilayer (SLB) system has allowed various parameters associated with the structure and function of membranes to be determined under quasi-physiological conditions [9, 10]. Using this system, we show that PIP$_2$ has significant effects both on membrane structure and on the resulting membrane–vesicle interaction. The second model system we used is the Langmuir film, where lipid molecules are spread on a buffer solution, forming a monolayer at the air–water interface [11]. The response of such a membrane, due to an interaction with SVs, can be investigated by measuring
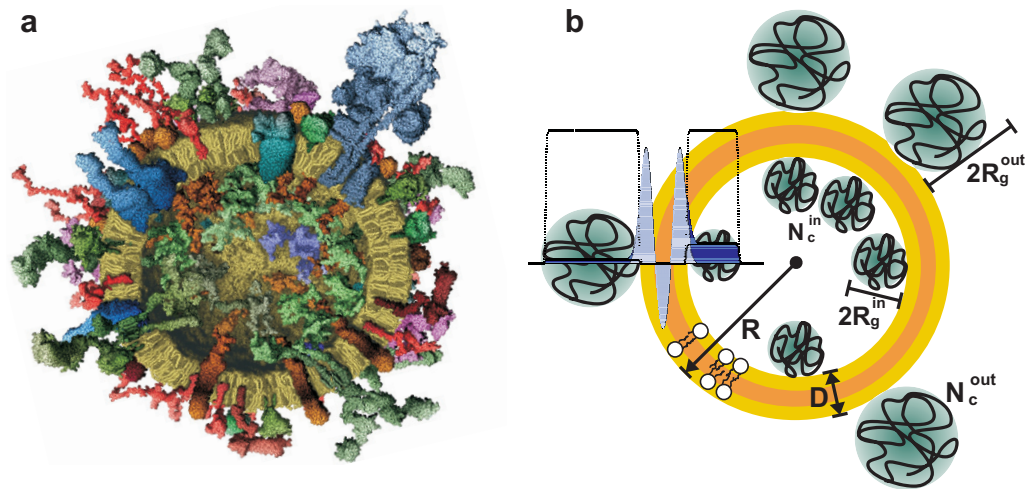
a   **b**

Figure 1. Schematic illustrations of the SV structure. (a) A cross-section of an average SV isolated from rat brain. This space-filling model is based mainly on a biochemical analysis of the lipid and protein composition. The size of the SV, however, was determined using cryo-electron microscopy (cryo-EM). The model is reprinted from [2], with permission from Elsevier. (b) Real-space model of an average rat SV derived from SAXS data. For details, see [3, 4] and also the text below.

the corresponding rearrangement of lipid molecules in the film following vesicle addition, in particular using the technique of grazing incidence x-ray diffraction (GIXD). Our GIXD data show considerable changes in the tilt angle of the alkyl chains, as well as changes in the lateral packing of lipids, following the association of SVs with the membrane—an effect that is again enhanced by the presence of PIP_2 in the membrane.

To summarize, the data presented here show that scattering techniques commonly applied in physics can play an important role in the study of membrane structure and function. Further, by using SVs as an effective calibration standard, we also directly demonstrate that these model membrane systems are capable of providing information at the level of whole organelles, an essential consideration when studying the mechanisms underlying membrane interactions and function.

2. Sample preparation

2.1. General chemicals

Lipid mono- and bi-layers were prepared from the following synthetic lipids: dioleoyl-*sn*-glycero-3-phosphatidylcoline (DOPC), dipalmitoyl-*sn*-glycero-3-phosphatidylcoline (DPPC) and PIP_2. In contrast, small spherical liposomes were prepared from brain-derived phosphatidyl-choline (PC), phosphatidylethanolamine (PE), phosphatidylserine (PS), phosphatidylinositol (PI) and cholesterol. All lipids were purchased as powders from Avanti Polar Lipids (Alabaster, AL). General chemicals were purchased from Sigma–Aldrich (Germany) and were of analytical grade or better. A stock solution of 1 M $CaCl_2$ and HB150 buffer (in mM: 150 KCl, 25 Hepes (pH 7.40 KOH) and 1 mM DTT) was made from salts using ultrapure water. Working solutions of $CaCl_2$ were made by an appropriate dilution of the 1 M stock solution into HB150. The final effective Ca^{2+} concentrations were verified using the fluorescent indicator dyes Fluo-5N and

Mag-Fura2 (Molecular Probes, Germany), against a standard curve constructed with a Molecular Probes calibration kit. Fluorescence measurements were made at 25 °C using a Fluoromax2 spectrophotometer (Jobin Yvon, Germany).

2.2. Synaptic vesicles (SVs)

SVs were purified from rat brain according to a protocol given in Takamori *et al* [2]. The dry weight of vesicles was calculated from the measured mass of the protein [12], considering that the protein and phospholipids comprising the vesicle are present in a 2 : 1 mass ratio [2]. The final mass concentrations of the vesicle preparation used were in the range of 4.5–5.4 g l^{-1}. Samples were snap-frozen and transported in a liquid nitrogen container to the experimental facility. SVs were then defrosted rapidly in a water bath at 37 °C before being used in experiments. Importantly, samples prepared and stored in this manner retain the capacity to acidify and store glutamate, an important indication that the samples are functionally intact.

2.3. Liposomes

Lipid stocks were prepared in a 2 : 1 (v/v) chloroform/methanol mixture. PC, PE, PS, PI and cholesterol were then mixed to get a final molar ratio of 5 : 2 : 1 : 1 : 1. After drying, this lipid mixture was then re-suspended in HB150 supplemented with 5% sodium cholate, to give a final lipid concentration of 13.5 mM. Liposomes were formed by gel filtration chromatography using either a SMART system with a PC3.2/10 Fast Desalting column (GE Healthcare, Germany) or a Bio-Rad EconoColumn filled with Sephadex G50 superfine (GE Healthcare).

2.4. Lipid monolayer at an air–water interface

A custom-made shallow Langmuir trough equipped with a single movable Teflon barrier was used to prepare the lipid monolayer at an air–water interface. Experiments were performed at ID10B of the European Synchrotron Radiation Facility (ESRF), Grenoble, France. Lipid stock solutions were prepared in a 20 : 9 : 1 (v/v) mixture of chloroform, methanol and water, giving a final lipid concentration of 0.2 g l^{-1}. About 75 μl of this stock solution was then spread onto a pure buffer solution, using a Hamilton syringe, to form the lipid monolayer. To ensure the complete evaporation of the organic solvent, compression was started 5 min after initial spreading of the lipid solution. The lipid monolayer was subsequently compressed or expanded with the Teflon barrier, using a velocity of 18 mm min^{-1}. First, the pressure–area isotherm was characterized for the various lipid compositions. The monolayers were compressed to a certain area per molecule, before the injection of SVs or liposomes into the subphase using a microloader. The final concentration of vesicles in the subphase was approximately 1.5 g l^{-1}.

2.5. Solid supported bilayer

DOPC and DOPC/PIP$_2$ were dissolved in the required amounts using a 20 : 9 : 1 (v/v) mixture of chloroform, methanol and water, after solvent removal using a vacuum oven. The resulting lipid film was then suspended in a buffer at a concentration of 2.5 g l^{-1}, followed by vortexing to yield a milky solution of lipids. Small unilamellar vesicles (SMVs) were prepared by sonication with a tip sonicator (Sonoplus, Germany) for approximately 15 min. To remove the titanium particles that were generated from the tip of the sonicator, the resulting lipid

solutions (which were now clear and transparent) were centrifuged in an Eppendorf bench-top centrifuge for 15 min at $14000 \, g_{Av}$. Lipid suspensions were subsequently diluted to a final concentration of $0.5 \, g \, l^{-1}$. Solid supported lipid bilayers were formed on cleaned (100)-silicon wafers (Silchem, Germany) by the fusion of SUVs. The wafers were initially cleaned using an ultrasonic bath that contained methanol, for two 15 min cycles, followed by three 15 min cycles in double-distilled water (18.2 MΩ cm, Millipore, USA). The wafers were then dried under a constant nitrogen flow, and their surfaces were rendered hydrophilic and made free from organic contaminants by etching using a plasma cleaner (Herrick Plasma, USA) for 4 min. A custom-made chamber, which held approximately 5 ml of HB150 buffer, was used for the x-ray reflectivity (XR) experiments [13]. The cleaned wafer ($15 \times 10 \, mm^2$) was placed in this chamber and approximately $750 \, \mu l$ of the final SUV solution was spread onto it. The sample was then incubated for 30 min. Excess vesicles were subsequently washed away using 20 ml of buffer. Importantly, membranes were kept hydrated for the duration of sample preparation and measurement. During the initial incubation of SUVs with the wafer and subsequent measurement, the chamber was placed in a heating system, which maintained a constant temperature of 40 °C using a glycol/water mixture originating from a temperature-controlled reservoir (Julabo, Germany). About $25 \, \mu l$ of SVs were then injected into the buffer on top of the bilayer, using a micropipette, and left for 30 min before experiments were started.

Figure 2 illustrates the various model systems used.

3. Experimental

3.1. Small angle x-ray scattering (SAXS)

SAXS measurements were performed either at the high-brilliance undulator beamline ID2 at ESRF or beamline B1 at the Doris III storage ring of HASYLAB (Deutsches Elektronen-Synchrotron, Hamburg, Germany). Beamlines were operated under the standard conditions of 12.4 keV [14] and 9.0 keV [15] photon energy, respectively. A simple schematic illustration of the experiment is shown in figure 3(a). SVs in HB150 buffer were kept in glass capillaries, which had a diameter of 1.5 mm and a wall thickness of 0.01 mm. The recorded data covered a q-range from approximately 0.016 to $5.5 \, nm^{-1}$ (ESRF) or from approximately 0.08 to $2.9 \, nm^{-1}$ (HASYLAB). Radiation damage was ruled out by the comparison of scattering patterns obtained with different exposure times. Dilution series revealed no measurable inter-particle correlations or aggregation for samples with total protein concentrations between 6.45 and $1.29 \, g \, l^{-1}$. Independently of SAXS, the relative size polydispersity $p(R)$ of the SV population was determined by cryo-EM. With this method, the vesicle radius R was determined by measuring from bilayer surface to bilayer surface. In total, 559 individual SVs were analyzed. Part of this work has been published previously in [3]. As a final confirmation of $p(R)$, dynamic light scattering measurements were also made (data not shown).

3.2. Scattering form factor model

The scattering cross-section for a dilute, polydisperse system of particles of radius R with number size distribution $p(R)$, volumes $V(R)$ and scattering form factor $P(q, R)$ is given by [16].

$$\frac{d\sigma(q)}{d\Omega} = \Delta\rho^2 \int_0^\infty p(R) V(R)^2 P(q, R) \, dR. \tag{1}$$
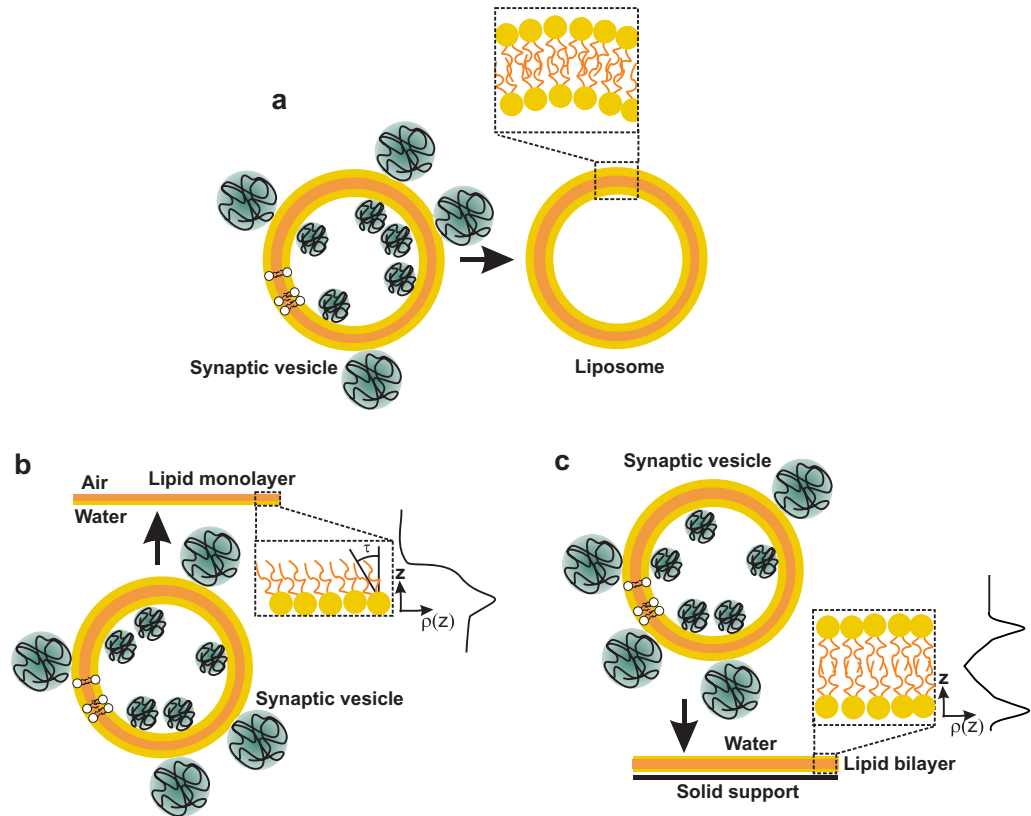
Figure 2. Schematic illustration of the various model systems used in these studies. (a) SVs and small lipid vesicles (liposomes) were incubated in a solution. (b) SVs were injected into the subphase of a lipid monolayer formed at the air–water interface. (c) SVs were introduced on top of a lipid bilayer formed on a solid support. The respective electron density profiles ($\rho(z)$) from the lipid monolayer and bilayer are also shown in (b) and (c), where the z-axis is parallel to the sample normal. τ is the tilt angle of the alkyl chains of the lipid molecules in the gel phase.

$V(R)$ is the dry volume of the particle defined as the total volume V_{tot} minus the volume of the solvent core V_{core}. A bimodal size distribution function $p(R)$ was employed in the SV models (see figure 4(b)). The branch of $p(R)$ centered on $R = 20$ nm was determined by cryo-EM (smoothed) [3], while the branch around $R = 200$ nm was calculated as a freely varied Gaussian contribution with mean μ and standard deviation σ. This factor accounts for the trace amounts of larger membranous particles that remain present in the sample following purification. The difference between the scattering length density of the solvent and the average scattering length density of the decorated bilayer is given by $\Delta\rho = M/V$. The form factor model was built from a central bilayer profile [17]–[19], with added contributions on the inside (lumen) and outside the membrane, to account for the protein components of the vesicle. The spherically symmetric electron density profile of the bilayer was modeled using three concentric Gaussians [20]. The symmetrical profile represents the headgroups of the two lipid leaflets, as well as the hydrophobic core of the bilayer. Protein residues associated with these lipid headgroups, as well as the transmembrane segments of vesicular proteins, are included in this contribution. Coronas
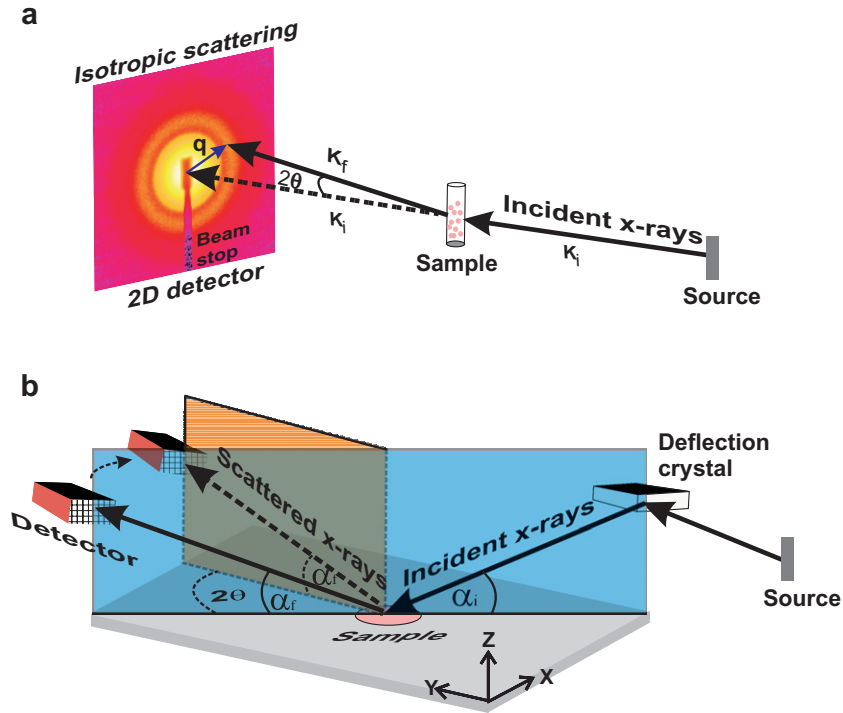
Figure 3. Schematic illustrations of the various equipment configurations used. (a) For SAXS measurement; the momentum transfer vector is given by $\vec{q} = \vec{K}_f - \vec{K}_i$ where $\vec{K}_f$ and $\vec{K}_i$ are the scattered and incident wave vectors. (b) For XR and GIXD measurements; during reflectivity measurements, the incident angle α_i is equal to the reflected angle α_f and $2\theta = 0$, whereas for GIXD $\alpha_i < \alpha_c$, where α_c is the critical angle at the interface and $2\theta \neq 0$. Both the monolayer and bilayer samples were prepared in the $x–y$ plane where the z-axis is parallel to the sample normal.

of Gaussian chains [21] attached to the inner and outer sides of the bilayer were used to model the larger proteins, or protein clusters, associated with the inside or outside of the SV, in a coarse-grained sense [3], [22]–[25]. Note that the contributions of the attached Gaussian chains explicitly introduced an in-plane structure to the model, which breaks the spherical symmetry. The individual Gaussian chains were assumed to be perfectly uncorrelated on the sphere, with no potential interactions existing. The local structure of the concentric bilayer profile and the additional terms describing the protein coronas were kept constant for all members of a polydisperse population. The effective number of free model parameters was 12. The model parameters were optimized by a least-squares fitting of the form factor to the SAXS data. Full details of the model and the fitting procedure have been published in [3].

3.3. Langmuir trough

A Langmuir trough with overall dimensions of $170 \times 210 \times 3\,\text{mm}^3$ was used for experiments, although the actual experimental area of the trough used depended on the position of a movable Teflon barrier. Before each experiment, the surface of the trough was carefully cleaned and then
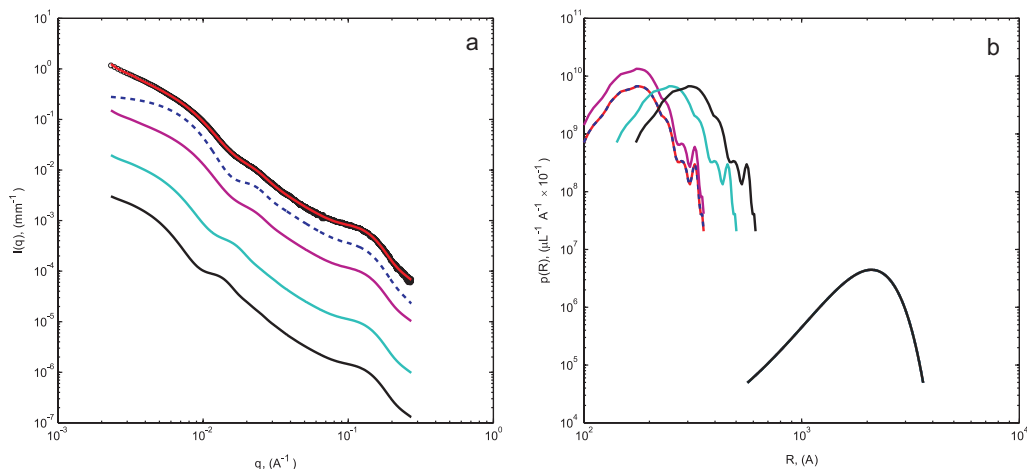
Figure 4. SAXS used for studying membrane structure. (a) SAXS data measured using SVs (○, black, $\times 10^0$), a model fit to the SAXS data (—, red, $\times 10^0$) and calculated scattering curves for proteoliposomes (PLs) (- - - -, blue, $\times 10^0$), a mixture of non-interacting SVs and PLs in a $1:1$ number ratio (—, violet, $\times 10^{-1}$), of SVs fused with PLs in a $1:1$ number ratio (—, green, $\times 10^{-2}$) and of SVs fused with PLs in a $1:2$ number ratio (—, black $\times 10^{-3}$). (b) Size distributions employed in the model calculations depicted in (a). The distribution on the right-hand side of the figure (plotted in black) is actually part of all the size distributions depicted by solid lines (—), except in the case of pure PLs (- - - -, blue).

checked by measuring the surface pressure of pure buffer solution. Only when the change in surface pressure was below $0.2\,\text{mN}\,\text{m}^{-1}$ was the trough used for experiments. The position of the Teflon barrier during experiments was controlled by ESRF electronics and integrated into the diffractometer control software (SPEC), which provides a software interface for the R&K electronic system (Riegler and Kirstein). Vesicle interaction with the lipid film was monitored by measuring the increase of interfacial pressure as a function of time, using a Wilhelmy balance with 10-mm-wide filter paper.

3.4. X-ray reflectivity (XR)

XR experiments on lipid monolayers were performed at the undulator beamline ID10B at ESRF. The incident wavelength λ was 1.55 Å with a beam size of $0.03 \times 0.1\,\text{mm}^2$. During both the reflectivity and the GIXD measurements, the Langmuir trough was placed on an active anti-vibration table. A linear position-sensitive detector (PSD; 150-mm-long Gabriel detector; EMBL, Grenoble, France) was used to collect the scattered beam coming from the interface. Measurements on both the DPPC and DPPC/PIP$_2$ monolayers were carried out at an interfacial surface pressure of $30\,\text{mN}\,\text{m}^{-1}$. Lipid bilayer experiments were performed using the Material Science (MS) beamline at the Swiss Light Source (SLS) in Villigen, Switzerland. The photon energy of the x-rays was set to 19 keV, with a beam cross-section of $0.2 \times 0.2\,\text{mm}^2$. A hexapod was used to precisely align the sample and the scattered photons were collected using a PILATUS II novel photon-counting 2D pixel detector. The scattered intensity was measured

as a function of incident angle α_i under specular conditions where the exit angle $\alpha_f = \alpha_i$ and the horizontal scattering angle $2\theta = 0$ (see figure 3(b)). Under these conditions, only the component q_z of the momentum transfer vector was obtained, where the z-axis is parallel to the sample normal. As every sample was exposed many times to collect data under different experimental conditions, radiation damage was avoided through a lateral translation of the sample between acquisitions. Furthermore, exposure times were precisely controlled using a fast shutter and a computer-controlled set of absorbers that were placed in front of the sample to limit exposure to the beam.

The XR from the interface of two media is characterized by the electron density profile $\rho(z)$ and is given by the master formula [26]

$$R(q_z) = R_F(q_z)| \int \frac{\mathrm{d}f(z)}{\mathrm{d}z} \, \mathrm{e}^{-\mathrm{i}q_z z} \mathrm{d}z|^2, \tag{2}$$

where $f(z) = \rho(z)/ \triangle \rho_{12}$ with $\triangle \rho_{12}$ being the density contrast between the media. The Fresnel reflectivity $R_F(q_z)$ from an ideal interface is expressed as $|(q_z - q_z')/(q_z + q_z')|$ with $q_z'^2 = q_z^2 - q_c^2$. In this study, the critical momentum transfer q_c is related to the critical angle at the air–water interface for the monolayer and at the water–Si substrate interface for the bilayer. In this paper, the data are analyzed with a box model, where each box is defined by its electron density (height) and thickness (width) [27, 28]. Both the height and the width of the boxes are taken as free parameters. The interfaces between the slabs are smeared with a finite value of surface roughness (maximum value $\sim 4.0\,\text{Å}$). Least-squares fits were performed using the simplex method implemented in the MATLAB Toolbox [29].

3.5. Grazing incident x-ray diffraction (GIXD)

GIXD measurements on the lipid monolayer were carried out using the undulator beamline ID10B at ESRF. During the experiments, a monochromatized x-ray beam was deflected at the downstream mirror to reach the angle of incidence, α_i, on the air–water interface. This angle was taken to be $0.8\alpha_c$, where α_c is the critical angle for total external reflection. For the wavelength $\lambda = 1.55\,\text{Å}$, $\alpha_c = 2.68\,\text{mrad}$. The diffracted beam was collected using a PSD (see figure 3(b)), with a Soller collimator mounted in front to define the horizontal resolution of the detector ($\triangle q_{xy} = 0.006\,\text{Å}^{-1}$). The scattered intensity was measured as a function of the horizontal scattering angle (2θ). The in-plane Bragg peaks were calculated from $q_{xy} = (4\pi/\lambda)\sin(2\theta/2)$. The scattered intensity recorded in channels along the detector also provided the q_z resolved Bragg rod profile. During both the reflectivity and GIXD measurements, the Langmuir trough was sealed and filled with water-saturated helium vapor to reduce the evaporation from the subphase and to avoid parasitic scattering from air. To be well below the chain-melting temperature of the lipid DPPC, all measurements on the monolayer were performed at $18\,^\circ\text{C}$. Otherwise, all conditions were identical to those used for the reflectivity measurements, with a surface pressure of $30\,\text{mN}\,\text{m}^{-1}$ being used.

Periodicity in the molecular arrangement of the monolayer plane can be calculated from the observed d-spacings, using the horizontal components q_{xy}^{hk} of the momentum transfer vector. From the primitive unit cell parameters a and b, the area per chain (A_I) can be obtained. If there is a tilt in the hydrocarbon chain from the layer normal, it can be calculated from the peak positions of q_{xy}^{hk} and the vertical component q_z^{hk}. In the case of an orthorhombic lattice, a non-degenerate peak (q^n) and a twofold degenerate peak (q^d) should be obtained. If the molecules

do not have any tilt, the vertical component (q_z^{hk}) of both of these peaks will vanish. A nearest-neighbor (NN) tilt produces $q_z^n = 0$ and $q_z^d > 0$, whereas a next-nearest-neighbor (NNN) tilt produces $q_z^n > 0$ and $q_z^d > 0$ [30]. In the present study, a single component is observed in the vertical peak, revealing an NN tilt of the lipid chain. The corresponding tilt angle (τ) is determined from [30, 31]

$$\tan(\tau) = \frac{q_z^d}{\sqrt{\left(q_{xy}^d\right)^2 - \left(\frac{q_{xy}^n}{2}\right)^2}}. \tag{3}$$

4. Results

4.1. SAXS from SVs and proteoliposomes

Our recent SAXS studies on SVs led to the publication of a low-resolution structural model of an average SV, as well as allowed us to determine the radial density profile $\rho(r)$, and the size polydispersity function $p(R)$, on an absolute scale with no free prefactors [3]. Importantly, our model form factor confirmed previous modeling studies of SVs, which were based solely on biochemical studies of the lipid and protein inventory, taking into account stochiometries of individual components, as well as their known structures [2]. However, the model further refined our structural picture of the SVs, as the model required the presence of laterally anisotropic structures on the vesicle surface, giving the first indication of large protein clusters in the membrane. Importantly, SAXS experiments allow the acquisition of structural data under quasi-physiological conditions, avoiding the invasive sample preparation steps needed for other techniques such as electron microscopy. Having obtained a basic model of SV structure, our aim is now to study changes in vesicle structure as a function of different physiological conditions—for example, pH, ionic strength and osmotic pressure are obvious candidates for further investigations [4]. Furthermore, it also appears that SAXS is suited to studying structural intermediates during the fusion of SVs with model membrane systems, such as protein containing liposomes, which substitute for the plasma membrane. It is hoped that in the future these experiments will provide insights into the fusion process that occurs *in vivo*.

To illustrate this point, here we consider calculated scattering curves and how they compare with SAXS data from SVs in a set of 'Gedankenexperiments'. In this theoretical exercise, SVs and proteoliposomes are mixed together and eventually fuse to form 'hybrid' vesicles. Conservation of SV and proteoliposome surface area is assumed during the fusion process. Furthermore, it is assumed that all particles in the two initial populations fuse and that the fusion probabilities are independent of the sizes of the fused particles, i.e. the population of 'hybrid' particles (fusion product) will exhibit, in general, a larger polydispersity than either of the two initial populations. We assume that the parameter values describing the local structure of the bilayers are conserved in all particles, both before and after fusion.

Figure 4(a) shows $I(q)$ versus q recorded for SVs in aqueous buffer (○, black) and a least-squares fit of a form factor model to the data (—, red), as published in [3]. The SAXS data can only be described by an anisotropic model, consisting of a symmetrical core profile (three concentric Gaussians) with attached Gaussian chains (solid red line), on both sides of the bilayer profile. A sketch of a real space model corresponding to the least-squares fit of the form factor is shown in figure 1(b). Pure proteoliposomes (- - - -, blue) were assumed to have similar bilayer structure, shape and size distribution to those used for the optimized SV model.

Unsurprisingly, this produced a similar scattering curve to the SAXS data obtained from SVs. However, since no larger contaminating particles are considered, the scattering curve levels off faster towards small q values, and the shoulder at $q \approx 2 \times 10^{-2}\,\text{Å}^{-1}$, which is due to the washed out first form factor minimum, is more pronounced. A mixture of non-interacting SVs and proteoliposomes (—, violet) produced a very similar calculated scattering curve when compared to the SAXS data for SVs alone. However, the feature at $q \approx 2 \times 10^{-2}\,\text{Å}^{-1}$ was somewhat more pronounced. In contrast, however, theoretical 'fusion assays', using either equal numbers of SVs and proteoliposomes or varying ratios, led to distinctly different scattering curves when compared with the measured SAXS data. The shoulder appearing at $q \approx 2 \times 10^{-2}\,\text{Å}^{-1}$ in the SAXS data moves significantly towards smaller q values, and gets increasingly pronounced.

Figure 4(b) shows the size polydispersity distribution functions $p(R)$ employed in the model calculations shown in figure 4(a). For all models involving SVs, a bimodal size polydispersity distribution function $p(R)$ was used, where one branch corresponds to cryo-EM data on the size distribution of SVs, proteoliposomes or the fusion products [32] and the second branch corresponds to larger membranous particles, which is modeled by an additional Gaussian distribution. Details of the SV form factor and the optimized parameter values obtained from the fit to the SAXS data, which have been used here, are given in [3, 4]. Interestingly, theoretical calculations show that the 'hybrid' fusion product shows a distinct SAXS profile when compared to those from either a non-interacting mixture of vesicles and proteoliposomes or experimental SAXS data obtained from vesicles only. Furthermore, it can be expected that even docking [33], or aggregation, of the SVs and liposomes would lead to distinct scattering patterns, making SAXS an ideal tool to discriminate between distinct structural intermediates in the fusion pathway, which are inaccessible to traditional techniques used to study membrane fusion, such as lipid dequenching assays.

4.2. Monolayer isotherm and interfacial pressure

In a further set of experiments, we aimed to try to understand the interactions of SVs with membranes, by using changes in interfacial pressure. Figure 5(a) shows the characteristic pressure–area isotherm of a pure DOPC monolayer measured at room temperature. The curve describes a single fluid phase, as this lipid has a chain-melting temperature of $-22\,°C$ [34]. Arrows mark the interfacial pressures at which SVs were injected into the subphase. The interaction of SVs with the monolayer was examined for various constant areas, by monitoring the change of interfacial pressure with time. Addition of SVs at an initial surface pressure (Π_i) of $10\,\text{mN}\,\text{m}^{-1}$ caused a dramatic increase in the interfacial pressure within a few minutes, followed by a much more gradual increase; overall, the interfacial pressure increased by 35% in 1 h. In contrast, a much slower and less pronounced effect was observed at $\Pi_i = 20\,\text{mN}\,\text{m}^{-1}$ (see figure 5(b)). At higher Π_i, it is to be expected that the lipid molecules are arranged more tightly in the film and, hence, the film is less sensitive to the addition of surface-active molecules. The most plausible explanation for the increase in surface pressure after the injection of SVs is the insertion of vesicle-associated proteins into the monolayer. Such an effect has previously been reported in the case of both green fluorescence protein (GFP) association with membranes and the insertion of anti-microbial peptides into lipid monolayers [35, 36]. The structural investigations discussed in the following sections further explain this observation.

Next, the interaction of liposomes with the DOPC monolayer was investigated by injecting them into the subphase under experimental conditions similar to those used for SVs. A plot
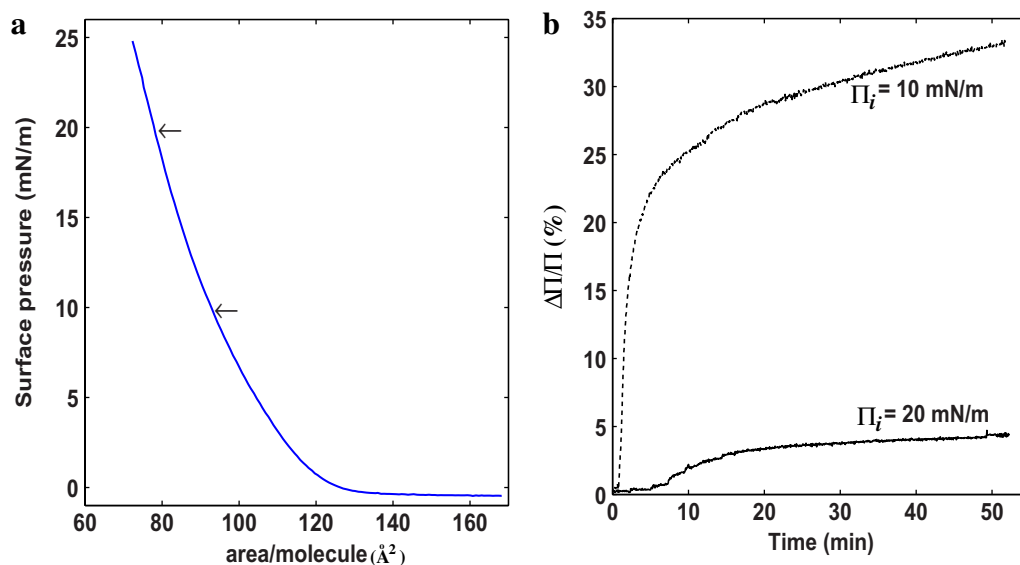
Figure 5. Representative pressure–area isotherm profiles. (a) Pressure–area isotherm of a DOPC monolayer on pure buffer. Arrows show the surface pressures at which vesicles were injected into the subphase. (b) Percentage change of surface pressure after SVs were injected into the subphase, at the two different initial surface pressures (Π_i) indicated in (a).

of the interfacial pressure obtained at $\Pi_i = 10\,\text{mN m}^{-1}$ is compared with the effect produced by SVs at the same pressure and is shown in figure 6(a). Note that the increase in surface pressure induced by liposomes was much less pronounced and reached a plateau very quickly ($\sim 5\,\text{min}$). Given that the lipid composition used to create these artificial vesicles is very similar to that found in native biological membranes, this experiment suggests that it is the SV-associated proteins that enhance the interaction of SVs with the monolayer. The slight increase in interfacial pressure resulting from the addition of pure lipid vesicles was expected from some reports in the literature, which suggest lipid migration from liposomes to the lipid film [37].

$\quad$ Ca^{2+} influx into the synaptic terminal is a critical event in the fusion of SVs with the plasma membrane. The influence of Ca^{2+} on the interaction of SVs with the lipoid film was easily studied by injecting $CaCl_2$ into the subphase. Estimates of the effective Ca^{2+} concentration needed to promote fusion vary, ranging from 10 to $100\,\mu\text{M}$. As a compromise, we added Ca^{2+} to an effective final concentration of $50\,\mu\text{M}$ [32]. The salt solution was injected approximately 1 h after the addition of SVs or liposomes to the system. Figure 6(c) shows the increase in surface pressure recorded over time after Ca^{2+} addition. Importantly, there was a more pronounced increase in interfacial pressure in the case of the DOPC/SV system compared with the DOPC/liposome system. This further increase in the surface pressure clearly indicates that Ca^{2+} enhances the interaction between the lipid monolayers and SVs/liposomes. Interestingly, a slight increase in interfacial pressure was also observed following the injection of $CaCl_2$, when vesicles were absent from the subphase, implying that Ca^{2+} causes structural changes in the monolayer itself, which may form the basis (at least partially) for the enhanced vesicle association (data not shown; [38]).
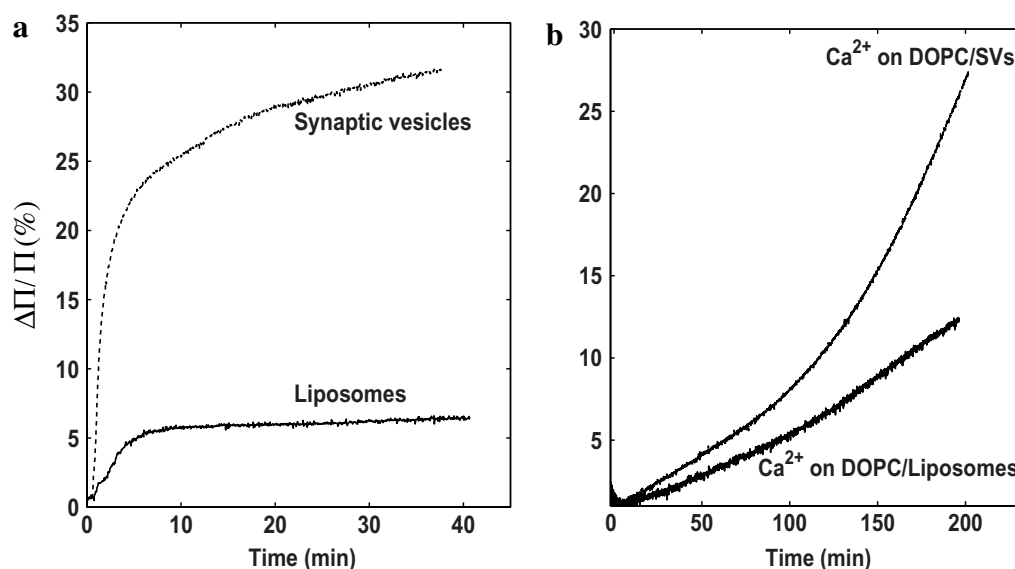
Figure 6. Changes in surface pressure of a monolayer, measured under various experimental conditions. (a) Changes in pressure after the injection of either SVs or liposomes into the subphase of a monolayer kept at a constant surface pressure of $\Pi_i = 10\,\mathrm{mN\,m^{-1}}$. (b) After 1 h of incubation with SVs or liposomes, $50\,\mu\mathrm{M}$ $CaCl_2$ was injected into the subphase. Note that although the surface pressure increased immediately in response to $CaCl_2$ injection, neither system reached equilibrium, even after 3 h.

4.3. XR measurements from a bilayer

We next aimed to study structural changes in a model membrane induced by SV association, using XR measurements. At the synapse, the most important lipid regulator of neurotransmitter release identified to date is PIP_2, which is thought to interact with the vesicular protein synaptotagmin—potentially playing a role in positioning of the vesicle at the release site. Hence, we decided to incorporate this molecule into lipid bilayers and record the outcome. In order to obtain clear 'proof-of-principle', we incorporated 20 mol% PIP_2 into the membrane. Although somewhat higher than the level previously recorded at the synapse ($\sim$ 6 mol%) [39, 40], this approach was taken to try to force an interaction between SVs and the model membranes during a first round of experiments. Such an artificial docking system also reflects the higher local concentration of the lipid at the active zone of SV fusion. Before investigating the interaction of SVs with the lipid bilayers, we first had to characterize DOPC and DOPC/PIP_2 membranes under similar experimental conditions, to establish whether incorporation of this lipid by itself elicited profound structural changes.

The reflectivity data for the bilayers were modeled using six so-called 'slabs' (six-box model fitting), with each slab representing one of the following: the outer headgroup, the hydrocarbon chain of the outer leaflet, the core region between the outer and inner leaflets, the hydrocarbon chain of the inner leaflet, the inner headgroup and the oxide (SiO_x) layer on top of the Si substrate. The solid lines in figure 7(a) are the fits corresponding to the electron density profiles shown in figures 7(b) and (c). From the resulting model of the DOPC bilayer, it appears that the electron density of the inner headgroup region ($0.59\mathrm{e^-\,\mathring{A}^{-3}}$) is higher than that of the
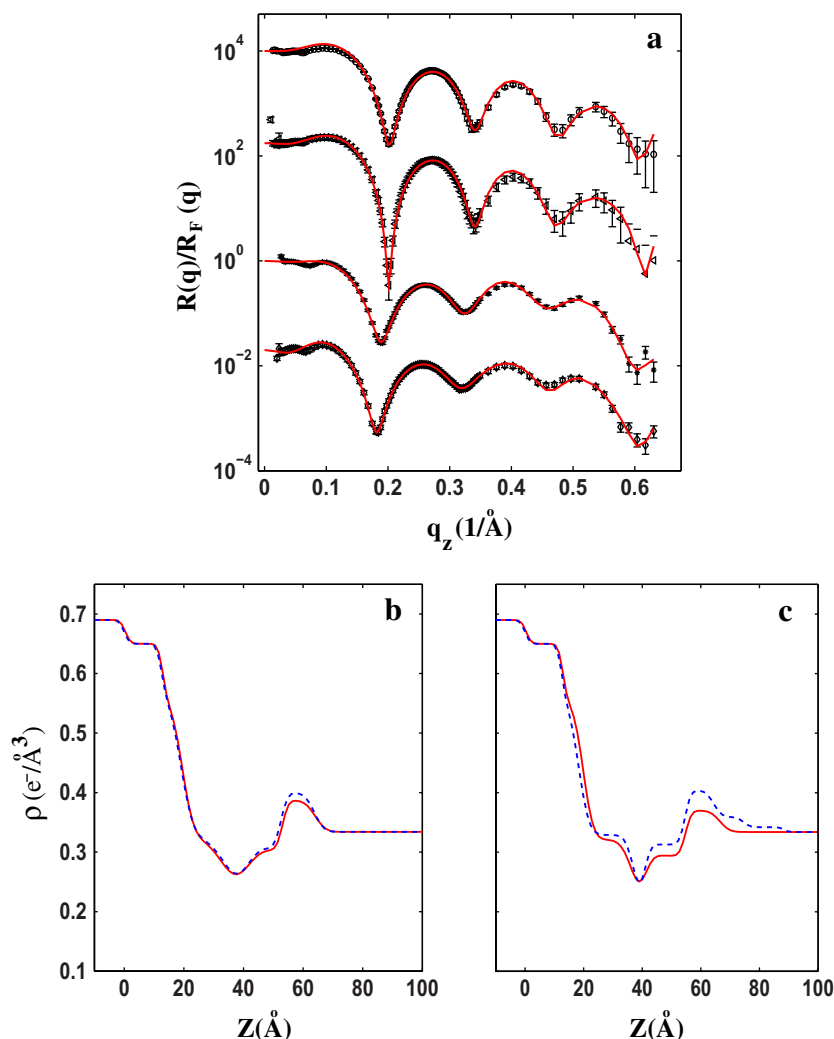
Figure 7. XR measurements from lipid bilayers. (a) Experimental data points (symbols) and fitted Fresnel normalized XR (solid lines): DOPC bilayer (○), DOPC bilayer with added synaptic vesicles (◁), DOPC/PIP$_2$ (4 : 1) bilayer (⋆) and DOPC/PIP$_2$ (4 : 1) bilayer with added SVs (◇). For clarity, the curves are shifted vertically. (b) Electron density profiles for a DOPC bilayer (solid line) and a DOPC bilayer with added SVs (dashed line). Both profiles are obtained using the six-box model fitting method. (c) Profiles for a DOPC/PIP$_2$ (4 : 1) bilayer fitted using a six-box model (solid line) and for a DOPC/PIP$_2$ (4 : 1) bilayer with added SVs fitted with an eight-box model (dashed line).

outer one ($0.39e^-$ Å^{-3}). Our calculated best fits require the bilayer to be separated from the substrate by a 12.5 Å thick SiO$_x$ layer, which contributes an electron density of $0.65e^-$ Å^{-3}, and it is this oxide layer that may 'contribute' electron density to the inner headgroup, explaining its comparatively high value in relation to the outer headgroup. The thickness of the outer headgroup region (11 Å) is higher than that of the inner one (6.6 Å). These values are in agreement with the literature values (10 and 8 Å, respectively) [41]. Although in some studies a water gap between the membrane and the support has been resolved [41, 42], in our analysis

such a water layer was not required to model the reflectivity data. Indeed, there are numerous other studies where such a water gap is also not considered [43]–[45]. In this kind of analysis, it is more reasonable to consider structural parameters associated with the outer leaflet of the bilayer, as the inner leaflet is always in close contact with the solid support, which might induce changes in the structure of the leaflet.

The presence of PIP_2 in the bilayer was evident from the shift in the minimum of the reflectivity profile towards lower q_z values, indicating a thickening of the lipid bilayer (see figure 7(a)). The best-fit profile yielded a bilayer thickness increase of 2.5 Å, in comparison with DOPC alone. The corresponding headgroup electron density was found to decrease slightly (0.01e$^-$ Å^{-3}), while the headgroup size was observed to increase by 0.8 Å, which is unsurprising given the bulky nature of the PIP_2 headgroup. Furthermore, PIP_2, which is negatively charged, is expected to form a rougher bilayer, which may also contribute to a larger headgroup value and an effectively lower electron density. From this analysis, however, we were not able to reach any conclusions about the spatial segregation of lipids in the film. As such, the possibility of small PIP_2 microdomains cannot be ruled out.

The reflectivity profiles obtained after addition of SVs to DOPC and DOPC/PIP_2 (4 : 1) bilayers are also shown in figure 7(a). The corresponding electron density profiles for the best fits are shown in figures 7(b) and (c), along with the measured electron densities of the bare bilayers for comparison. The reflectivity profile of the DOPC/SV bilayer is very similar to that of DOPC alone, except for the cusp observed in the first minimum. The data were modeled using a 'six-slab' approach and revealed a slight increase in electron density across the bilayer. In the case of the DOPC/PIP_2/SV system, the data could only be modeled with the use of an additional two slabs. This 'eight-slab model' was then able to accurately reproduce the reflectivity data. The increases in electron densities measured at both the head and tail regions were found to be 0.035e$^-$ and 0.019e$^-$ Å^{-3} when compared with the bare DOPC/PIP_2 bilayer. For the DOPC/SV system, the corresponding increases were 0.012e$^-$ and 0.002e$^-$ Å^{-3}, respectively. We think that the two extra slabs needed to accurately model the reflectivity data represent vesicle-associated proteins with electron densities of 0.36e$^-$ and 0.34e$^-$ Å^{-3} and respective sizes of 10 and 11 Å. Interestingly, the increase in electron density across the DOPC/PIP_2 bilayer is much more pronounced than that of the DOPC membrane, indicating a stronger interaction of SVs with the membrane in the presence of PIP_2. In future, however, experiments will have to concentrate on titration of the PIP_2 level and assessment of the vesicle–membrane interaction under more physiologically relevant conditions. Such an experiment with variable amounts of PIP_2 is a very worthwhile extension of this work.

4.4. XR measurements from a monolayer

All of the reflectivity data obtained from the monolayer system were fitted with a two-box model: one box corresponding to the headgroup region of the lipid component and the other to the tail. The electron densities of the subphase and the air were taken to be 0.334e$^-$ Å^{-3} and zero, respectively. For a pure DPPC monolayer, the measured headgroup electron density was 0.42e$^-$ Å^{-3}, while the hydrocarbon chain electron density was 0.29e$^-$ Å^{-3}. The total film thickness was approximately 24 Å. These structural parameters were used as the starting point for the subsequent fitting of data obtained after SVs had been injected into the subphase. In fact, a slightly different electron density profile from that of pure DPPC was obtained after addition of SVs. The data and the fit are described in figure 8(a), with the corresponding electron density
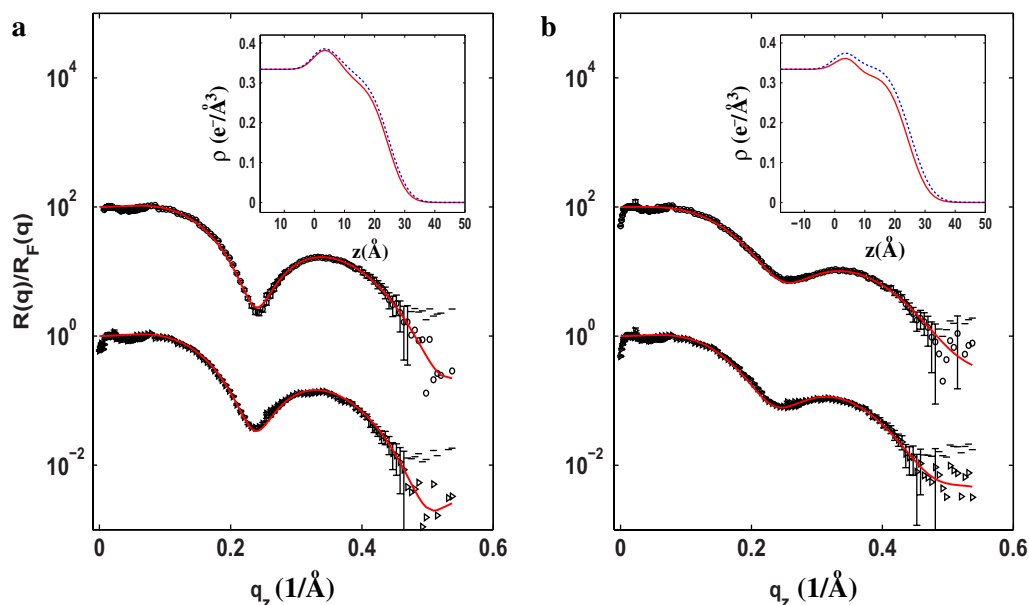
Figure 8. XR measurements from lipid monolayers. (a) DPPC monolayer (○) and DPPC monolayer after injection of SVs into the subphase (▷). (b) DPPC/PIP$_2$ (19:1) monolayer (○) and DPPC/PIP$_2$ (19:1) monolayer with SVs (▷). The normalized Fresnel XR curves are shown by solid lines. For clarity, the curves are shifted vertically. Inset: the corresponding electron density profiles before (solid line) and after (dashed line) injection of SVs into the subphase.

profiles shown in the inset. Note that we did not need to introduce any extra slabs to reproduce the reflectivity curve when SVs were present in the subphase. In fact, the interaction of vesicles with these lipid monolayers resulted in only a slight increase in the electron density across the lipid film and also a slight increase in the film thickness (approximately 1 Å). Such a small change in these structural parameters reflects a correspondingly weak interaction between the SVs and the lipid monolayer. Although the change in interfacial pressures observed using a DOPC monolayer is suggestive of a stronger interaction, it should be remembered that in these experiments the lipid layers were at much lower surface pressures, where the molecules are loosely packed, and vesicles were more likely to physically interact.

In the case of our monolayer experiments, we have already been able to titrate the level of PIP$_2$ in the membrane down to 5 mol%, a figure that is thought to reflect the physiological level of this lipid at discrete sites on the presynaptic plasma membrane [46]. Figure 8(b) shows reflectivity data obtained from a DPPC/PIP$_2$ monolayer and a DPPC/PIP$_2$ monolayer after injection of SVs into the subphase. Both data sets were again fitted with a two-box model. As also observed in the single lipid bilayer experiments, the presence of PIP$_2$ in the monolayer produced a reflectivity curve that was best fitted with a lower electron density for the headgroup when compared with the pure DPPC monolayer ($\Delta\rho = 0.03\mathrm{e}^-$ Å^{-3}). Following the injection of SVs, the reflectivity data were indicative of distinctly different structural parameters. They exhibited higher electron densities both in the head and chain regions of the lipid film. From an inspection of figures 8(a) and (b), it can be readily observed that such an increase was more pronounced in the DPPC/PIP$_2$ monolayer than in the monolayer comprised solely of DPPC. Following the injection of SVs into the subphase, the DPPC/PIP$_2$ film was thickened

by ~ 2 Å, whereas the DPPC film was only thickened by ~ 1 Å. Hence, the presence of PIP$_2$ in the monolayer enhanced the interaction of SVs with the lipid film, an observation that is further supported by the reflectivity experiments performed on single lipid bilayers (see above) and the grazing incident x-ray diffraction experiments that are explained in the section below.

The presence of an extra macromolecular layer above the lipid bilayer is generally indicated by a requirement for more slabs in the box model [47]. In the case of a monolayer, such an extra layer would be observed below the lipid film in the subphase [48, 49], and the electron density of such a continuous layer would correspond to the electron density of the macromolecules. However, in the present study, we have much more indirect evidence for the presence of SVs near the lipid interface, reflected by the structural changes induced in the lipid layer itself. The most widely accepted space-filling model of SVs (diameter ~ 420 Å) suggests that the lipid bilayer of SVs is decorated with proteins [2], organized into discrete microdomains [3]. In our previous SAXS study, SVs were modeled as unilamellar vesicles with added protein domains. In the model, these domains were represented using Gaussian chains. The best fit to the model yielded 12.9 Gaussian chains on the inside (radius of gyration approximately 32 Å) and 4.2 Gaussian chains on the outside (approximate radius of gyration 57 Å) (see figure 1(b)) [3]. Thus, proteins on the outside of the SV would contribute to a 'protein layer' near the lipid interface after docking. However, even with a closely packed arrangement of vesicles near the lipid layer, we estimate that only 5–15% of the surface area of the lipid layer would be covered by vesicle-associated proteins. This was calculated taking into account the different positions of the Gaussian chains on the surfaces of the SVs in our sample and the surface area of the lipid membrane used. In itself, this low surface coverage should not significantly change the average electron density in the plane immediately above the lipid bilayer or below the lipid monolayer. Instead, changes in the electron density profiles $\rho(z)$ are best explained by a non-local and collective reorganization of the membrane in response to the local adsorption of SVs to the membrane, via insertion of their associated proteins. Indeed, a large increase in electron density was observed both in the headgroup region and in the hydrophobic region. However, the changes in $\rho(z)$ were significantly stronger when PIP$_2$ was incorporated into the membrane. Thus, PIP$_2$ increases the binding affinity of SVs to the membranes. It is worth noting, however, that the specificity of this interaction is still not fully resolved by these results. Firstly, other interface active ions or molecules may also show strong effects in modulating the membrane–vesicle interaction in the presynaptic terminal. Secondly, such molecules may even lead to comparatively large structural changes in the plasma membrane in the complete absence of SVs.

4.5. GIXD measurements from a monolayer

In light of our XR data showing an interaction of SVs with model membranes, we decided to use GIXD to try and determine the structural changes in the membrane underlying this association. As GIXD is most sensitive to a gel phase with long-range ordering of the alkyl chains, we used the lipid DPPC to form monolayers. DPPC was chosen because it has a chain melting temperature of ~ 41 °C [50], which is significantly higher than our measuring temperature of 18 °C—while the phases formed by DPPC at various surface pressures are also well studied and understood [51]–[53]. The molecular packing parameters determined for this lipid were used as the starting point for our investigations into the interaction of SVs with a DPPC monolayer with and without additional PIP$_2$.
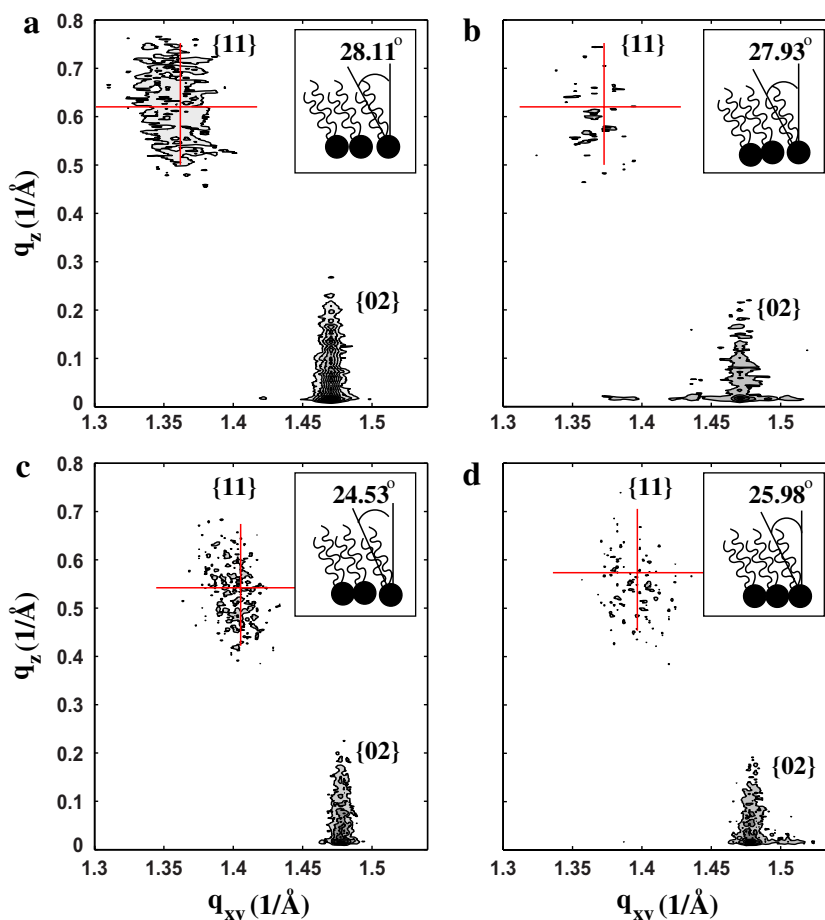
Figure 9. Contour plots from GIXD measurements performed on lipid monolayers. (a) DPPC monolayer only. (b) DPPC monolayer with SVs injected into the subphase. (c) DPPC/PIP$_2$ monolayer. (d) DPPC/PIP$_2$ monolayer with SVs in the subphase. Corresponding tilt angles of the lipid molecules are shown in the inset. Crosses indicate the positions of the peaks.

The contour plots of our GIXD data are shown in figure 9, in which both q_{xy} and q_z are resolved. Two diffraction Bragg peaks were observed in all of the samples we studied (see figure 10). These peaks were indexed as (11) and (02), indicating a centered rectangular unit cell [51]. Note that the centered rectangular lattice can also be interpreted as a distorted hexagonal lattice. The chains are tilted towards their nearest neighbor. For the condensed phase of DPPC, at a surface pressure of 30 mN m^{-1}, the lattice parameters of the unit cell were found to be 5.45 and 8.54 Å, providing an area per chain of $A_I = 23.32$ Å^{-2}. The corresponding tilt angle was calculated to be 28.11°, which is a little lower than that previously published ($\sim$30°) [52, 53], although this could be an effect of the buffer solution used in the subphase.

The Bragg peaks obtained when SVs were injected into the subphase of a pure DPPC monolayer are shown in figure 10. Here, two distinct Bragg peaks again indicate a rectangular unit cell with very similar lattice parameters compared with pure DPPC alone. The area per chain and the tilt angle of the chain were found to be almost identical (table 1). Hence, the presence of SVs in the subphase did not produce a major reorganization of the lipid chains
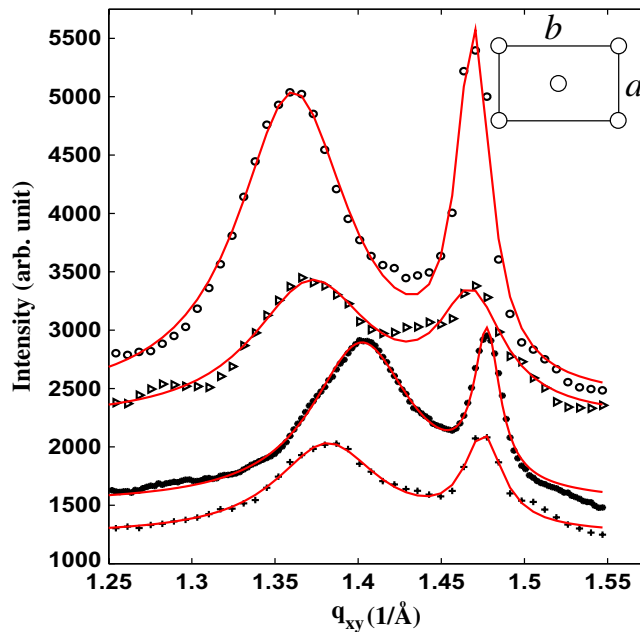
Figure 10. GIXD measurements on DPPC monolayers: DPPC monolayer (○), DPPC monolayer after injection of SVs into the subphase (▷), DPPC/PIP$_2$ monolayer (●) and DPPC/PIP$_2$ monolayer with SVs (+). The Bragg peaks are least-squares fits of two Lorentzians (solid lines). The centered rectangular unit cell is illustrated in the inset. For clarity, the curves are shifted vertically.

Table 1. Structural parameters of lipid monolayers obtained from GIXD measurements. Here, d_{11} and d_{02} are the d-spacings; a and b are the dimensions of the rectangular unit cell; A_I is the area per chain; and τ is the tilt angle of the alkyl chain.

Sample	d_{11} (Å)	d_{02} (Å)	a (Å)	b (Å)	A_I (Å^2)	τ (deg)
DPPC	4.59	4.27	5.45	8.54	23.32	28.1
DPPC/SV	4.57	4.27	5.42	8.55	23.16	27.9
DPPC/PIP$_2$	4.47	4.25	5.26	8.51	22.38	24.5
DPPC/PIP$_2$/SV	4.51	4.25	5.32	8.50	22.65	25.9

in the film, unlike when bacterial surface (S)-layer proteins 'couple' to lipid monolayers [54]. However, the addition of SVs did decrease the peak intensities and also led to a broadening of the peaks [52, 55], which could reflect disorder and strain associated with the partial binding of vesicles. Even a low fraction of adsorbed SVs could explain such an effect. This minor effect on chain organization is reminiscent of the weak vesicle–membrane interaction we observed in reflectivity measurements when PIP$_2$ was absent.

Hence, next we included a small, physiologically relevant amount of PIP$_2$ (5 mol%) in our DPPC monolayers, and observed a corresponding shift in the Bragg peaks towards higher q_{xy} values, indicating a smaller rectangular unit cell (see figures 9(c) and 10; table 1). The area per chain in this DPPC/PIP$_2$ monolayer was 22.38 Å^2 and the corresponding tilt angle was 24.5°, indicating that a small amount of PIP$_2$ was sufficient to induce a measurable structural

change in the membrane. Interestingly, after injection of SVs into the subphase, both Bragg peaks shifted towards lower q_{xy} values, revealing a bigger unit cell with parameters of 5.32 and 8.50 Å, an area per chain of 22.65 Å^2 (which is higher than DPPC/PIP$_2$ alone) and a chain tilt of 25.98°. Obviously, therefore, the addition of SVs has opposite effects on the tilt angle, depending on whether PIP$_2$ is present or absent from the membrane. At the moment, we are unable to elaborate further on the mechanistic basis of this observation, which is currently under investigation. However, these data do reinforce the concept that PIP$_2$ plays an important role in SV–membrane interaction, consistent with our reflectivity measurements on both lipid monolayers and bilayers.

5. Discussion

Using SVs as a model system, we investigated whether commonly used scattering techniques could be used to investigate structure–function relationships during membrane fusion. Not only did 'proof-of-principle' experiments demonstrate that these types of experiment are possible, but in themselves they also provided useful results that will form the basis of continuing investigations in our laboratory over the coming years.

For instance, as a result of our theoretical calculations concerning the fusion of SVs and proteoliposomes, SAXS will be used to try and identify distinct structural intermediates in the fusion pathway. The major effect of PIP$_2$ on membrane structure, including the thickening of the bilayer and a reduction in electron density, was particularly surprising to us. In particular, we plan to investigate how these structural changes relate to the enhanced interaction of SVs with membranes in the presence of PIP$_2$. Known membrane proteins on the vesicle include synaptotagmin, which is thought to act as the Ca^{2+} sensor during exocytosis. Although we can make no direct judgment, it is tempting to speculate that synaptotagmin is responsible for mediating the interaction between vesicles and the membrane. Firstly, synaptotagmin is a major vesicle protein (each vesicle contains, on average, 15 copies of synaptotagmin 1, which considering the presence of other isoforms is likely to be an underestimate [2]). Secondly, synaptotagmin is known to interact with PIP$_2$ at concentrations of calcium required for transmitter release [56]. Although PIP$_2$ is known to play an important role in vesicle association with membranes, future experiments will also have to consider that proteins such as synaptotagmin have multiple molecular partners at the synapse. For instance, as well as associating with membranes, synaptotagmin also interacts with the plasma membrane SNARE proteins syntaxin 1 and SNAP-25, which, together with the vesicular protein synaptobrevin, are thought to constitute the minimal machinery needed for membrane fusion at the release site [57]. Unfortunately, to date it has been impossible to reconstitute the 'docked' state of an SV with a membrane *in vitro*, as incorporation of SNARE proteins into artificial membranes inevitably leads to fusion. However, only by understanding this 'docked' state will we be able to fully understand the fusion pathway from initial vesicle recruitment to the final membrane merger. Therefore, syntaxin and SNAP-25 will eventually have to be reconstituted into membranes in a way in which vesicles remain stably associated until Ca^{2+} addition. This will allow us to investigate the specific roles of these proteins in fusion, with particular emphasis on the structural changes that result in the membrane. However, given the risk of protein–solid support interactions, it is envisaged that this type of experiment would require the use of a soft polymer cushion. In fact, the recent development of the so-called 'soft-supported bilayers' opens up the possibility of performing these experiments [58].

As a final thought, the activation energy needed to fuse two membranes is not yet known precisely, with estimates ranging widely from 40 to 200 $k_B T$ [59, 60], although recent *in vitro* experiments indicate that sufficient energy to fuse a SV with a membrane can be provided by a single SNARE protein complex [61]. However, it is interesting to speculate that a conformational change in the plasma membrane, induced by *de novo* synthesis of PIP_2 and Ca^{2+} influx into the nerve terminal, may also play a role in reducing the activation energy needed for fusion *in vivo*. The non-local and collective reorganization of the membrane we have shown here could be associated with high free energy changes, and may contribute to the apparent nonlinearity of vesicle fusion at multiple sites across the active zone of the synapse [62].

6. Conclusion

We have shown results from three complementary x-ray scattering techniques with the aim of illustrating their suitability for studying the structure and functional interaction of SVs with lipid membranes. First, we presented the SAXS analysis of the SV structure, alongside a theoretical consideration of the applicability of SAXS to study the intermediate structural states of the fusion pathway. In addition, using the known interaction of SVs with the membrane lipid PIP_2, we have also shown that both XR and grazing incidence diffraction have great promise in studying the interactions of trafficking organelles with their target membranes. As we have observed in this study, these techniques are capable of providing unprecedented structural insight into such interactions. In future, we envisage using model membranes of increasing complexity, as well as liposomes containing purified vesicular components, to try to elucidate the identity and function of membrane-interacting components. As it is now recognized that many principles of membrane trafficking are conserved between the various cellular pathways, we hope that results determined with this system will have applicability to questions of membrane trafficking in general.

Acknowledgments

References

[1] Südof T C 2004 *Annu. Rev. Neurosci.* **27** 509
[2] Takamori S *et al* 2006 *Cell* **127** 831
[3] Castorph S, Riedel D, Arleth L, Sztucki M, Jahn R, Holt M and Salditt T 2010 *Biophys. J.* **98** 1200
[4] Castorph S, Arleth L, Sztucki M, Vainio U, Ghosh S K, Holt M, Jahn R and Salditt T 2010 *J. Phys: Conf. Ser.* in press

[5] Chapman E R 2008 *Annu. Rev. Biochem.* **77** 615

[6] Woodbury D J and Rognlien K 2000 *Cell Biol. Int.* **24** 809

[7] McNew J A, Weber T, Parlati F, Johnston R J, Melia T J, Söllner T H and Rothman J E 2000 *J. Cell Biol.* **150** 105

[8] Paolo G D, Moskowitz H S, Gipson K, Wenk M R, Voronov S, Obayashi M, Flavell R, Fitzsimonds R M, Ryan T A and Camilli P D 2004 *Nature* **431** 415

[9] Tamm L K and McConnell H M 1985 *Biophys. J.* **47** 105

[10] Sackmann E 1996 *Science* **271** 43

[11] Möhwald H 1990 *Annu. Rev. Phys. Chem.* **41** 441

[12] Peterson G L 1977 *Anal. Biochem.* **83** 346

[13] Nováková E, Giewekemeyer K and Salditt T 2006 *Phys. Rev.* E **74** 051911

[14] Narayanan T, Diat O and Boesecke P 2001 *Nucl. Instrum. Methods Phys. Res.* A **467** 1005

[15] Haubold H-G *et al* 1989 *Rev. Sci. Instrum.* **60** 1943

[16] Guinier A and Fournet G 1955 *Small Angle Scattering of X-Rays* (New York: Wiley Interscience)

[17] Bouwstra J A, Gorris G S, Bras W and Talsma H 1993 *Chem. Phys. Lipids* **64** 83

[18] Pabst G, Rappolt M, Amenitsch H and Laggner P 2000 *Phys. Rev.* E **62** 4000

[19] Pabst G, Koschuch R, Pozo-Navas B, Rappolt M, Lohner K and Laggner P 2003 *J. Appl. Cryst.* **36** 1378

[20] Gradzielski M, Langevin D, Magid L and Strey R 1995 *J. Phys. Chem.* **99** 13232

[21] Debye P 1947 *J. Phys. Colloid Chem.* **51** 18

[22] Pedersen J S and Gerstenberg M C 1996 *Marcromolecules* **29** 1363

[23] Pedersen J S 2000 *J. Appl. Cryst.* **33** 637

[24] Pedersen J S 2001 *J. Chem. Phys.* **114** 2839

[25] Arleth L and Vermehren C 2010 *J. Appl. Cryst.* **43** 1084

[26] Als-Nielsen J and McMorrow D 2001 *Elements of Modern X-Ray Physics* (Chichester: Wiley)

[27] Strzalka J, DiMasi E, Kuzmenko I, Gog T and Blasie J K 2004 *Phys. Rev.* E **70** 051603

[28] Hohage T, Giewekemeyer K and Salditt T 2008 *Phys. Rev.* E **77** 051604

[29] Giewekemeyer K 2006 *Diploma Thesis* University of Goettingen, Goettingen, Germany

[30] Kaganer V M, Möhwald H and Dutta P 1999 *Rev. Mod. Phys.* **71** 779

[31] Andreeva T D, Petrov J G, Brezesinski G and Möhwald H 2008 *Langmuir* **24** 8001

[32] Holt M, Riedel D, Stein A, Schuette C and Jahn R 2008 *Curr. Biol.* **18** 715

[33] Cypionka A, Stein A, Hernandez J M, Hippchen H, Jahn R and Walla P 2009 *Proc. Natl Acad. Sci. USA* **106** 18575

[34] Edmiston P L and Saavedra S S 1998 *Biophys. J.* **74** 999

[35] Prachayasittikul V, Ayudhya C I N, Boonpangrak S and Galla H-J 2004 *J. Membr. Biol.* **200** 47

[36] Gidalevitz D, Ishitsuka Y, Muresan A S, Konovalov O, Waring A J, Lehrer R I and Lee Y C 2003 *Proc. Natl Acad. Sci. USA* **100** 6302

[37] Marchi-Artzner V, Lehn J-M and Kunitake T 1998 *Langmuir* **14** 6470

[38] Ghosh S K, Castorph S, Konovalov O, Jahn R, Holt M and Salditt T unpublished

[39] James D J, Khodthong C, Kowalchyk J A and Martin T F J 2008 *J. Cell Biol.* **182** 355

[40] Hay J C, Fisette P L, Jenkins G H, Kukami K, Takenawa T, Anderson R A and Martin T F J 1995 *Nature* **374** 173

[41] Miller C E, Majewski J, Gog T and Kuhl T L 2005 *Phys. Rev. Lett.* **94** 238104

[42] Watkins E B, Miller C E, Mulder D J, Kuhl T L and Majewski J 2009 *Phys. Rev. Lett.* **102** 238101

[43] Hochrein M B, Reich C, Krause B, Rädler J O and Nickel B 2006 *Langmuir* **22** 538

[44] Reich C, Hochrein M, Krause B and Nickel B 2005 *Rev. Sci. Instrum.* **76** 095103

[45] Miller C E, Majewski J, Watkins E B, Mulder D J, Gog T and Kuhl T L 2008 *Phys. Rev. Lett.* **100** 058103

[46] McLaughlin S and Murry D 2005 *Nature* **438** 605

[47] Horton M R, Reich C, Gast A P, Rädler J O and Nickel B 2007 *Langmuir* **23** 6263

[48] Struth B, Rieutord F, Konovalov O, Brezeinski G, Grübel G and Terech P 2002 *Phys. Rev. Lett.* **88** 025502

[49] Cristofolini L, Berzina T, Erokhina S, Konovalov O and Erokhin V 2007 *Biomacromolecules* **8** 2270

[50] Abrams S B and Yager P 1993 *Biochim. Biophys. Acta* **1146** 127

[51] Lee K Y, Gopal A, Nahmen A V, Zasadzinski J A, Majewski J, Smith G S, Howes P B and Kjär K 2002 *J. Chem. Phys.* **116** 774

[52] Wu G, Majewski J, Ege C, Kjär K, Weygand M J and Lee K Y 2005 *Biophys. J.* **89** 3159

[53] Brezesinski G, Dietrich A, Struth B, Böhm C, Bouwman W G, Kjär K and Mhwald H 1995 *Chem. Phys. Lipid* **76** 145

[54] Weygand M, Wetzer B, Pum D, Sleytr W B, Cuvillier N, Kjaer K, Howes P B and Lösche M 1999 *Biophys. J.* **76** 458

[55] Konovalov O, Myagkov I, Struth B and Lohner K 2002 *Biophys. J.* **31** 428

[56] Schiavo G, Gu Q, Prestwich G D, Soellner T H and Rothman J E 1996 *Proc. Natl Acad. Sci. USA* **93** 13327

[57] Jahn R, Lang T and Südhof T C 2003 *Cell* **112** 519

[58] Smith H L, Jablin M S, Vidyasagar A, Saiz J, Watkins W, Toomey R, Hurd A J and Majewski J 2009 *Phys. Rev. Lett.* **102** 228102

[59] Kozlovsky Y, Chernomordik L V and Kozlov M M 2002 *Biophys. J.* **83** 2634

[60] Siegel D P and Kozlov M M 2004 *Biophys. J.* **87** 366

[61] van den Bogaart G, Holt M G, Bunt G, Riedel D, Wouters F S and Jahn R 2010 *Nat. Struct. Mol. Biol.* **17** 358

[62] Schneggenburger R and Neher E 2005 *Curr. Opin. Neurobiol.* **15** 266